

pubs.acs.org/acscatalysis Research Article

Controlled Trafficking of Multiple and Diverse Cations Prompts Nucleic Acid Hydrolysis

Jacopo Manigrasso, Marco De Vivo,* and Giulia Palermo*



Cite This: ACS Catal. 2021, 11, 8786-8797



Read Online

ACCESS

III Metrics & More



SI Supporting Information

ABSTRACT: Recent *in crystallo* reaction intermediates have detailed how nucleic acid hydrolysis occurs in the RNA ribonuclease H1 (RNase H1), a fundamental metalloenzyme involved in maintaining the human genome. At odds with the previous characterization, these *in crystallo* structures unexpectedly captured multiple metal ions (K^+ and Mg^{2+}) transiently bound in the vicinity of the two-metal-ion active site. Using multi-microsecond all-atom molecular dynamics and free-energy simulations, we investigated the functional implications of the dynamic exchange of multiple K^+ and Mg^{2+} ions at the RNase H1 reaction center. We found that such ions are timely positioned at nonoverlapping locations near the active site, at different stages of catalysis, being crucial for both reactants' alignment and



leaving group departure. We also found that this cation trafficking is tightly regulated by variations of the solution's ionic strength and is aided by two conserved second-shell residues, E188 and K196, suggesting a mechanism for the cations' recruitment during catalysis. These results indicate that the controlled trafficking of multication dynamics, opportunely prompted by second-shell residues, is functionally essential to the complex enzymatic machinery of the RNase H1. These findings improve the current knowledge on the catalysis of the RNase H1 andopen new catalytic possibilities for other metalloenzymes including, but not limited to, CRISPR-Cas9, group II intron ribozyme and the human spliceosome.

KEYWORDS: cations, second-shell residues, positive-charge trafficking, nucleic acid processing, catalysis, molecular dynamics

■ INTRODUCTION

Recently, structural and biophysical studies have revealed that additional metal ions (viz, K^+ and Mg^{2+}) are transiently engaged in the vicinity of the well-recognized two-metal-ion catalytic site of enzymes like DNA/RNA polymerases, 1,2 endo-and exonucleases, $^{3-6}$ and even type II topoisomerase. $^{7-9}$ All these metalloenzymes are fundamental for the expression and maintenance of RNA and DNA within the cell $^{10-12}$ and are often targeted to treat human diseases from cancer to viral and bacterial infections. $^{13-16}$

Remarkably, transient K⁺ and Mg²⁺ ions have been often captured unexpectedly close to conserved second-shell protein residues, which have been thereby proposed to favor metal recognition and recruitment from the bulk.¹⁷ Such positive ions at the metal-aided catalytic site during the processing of nucleic acids were suggested to contribute actively to the overall catalytic process, ^{1,18–24} although their exact functional and dynamic role remains only partially understood.

In this context, the prototypical nucleic acid processing enzyme RNA ribonuclease H1 (RNase H1, Figure 1A), which cleaves the phosphodiester bond in RNA:DNA hybrids being responsible for removing the Okazaki fragments during DNA replication, has been extensively characterized via biophysical and computational studies.

Nevertheless, only recent data, obtained using time-resolved X-ray crystallography, ³⁶ have shown that the catalysis of RNase

H1 is accompanied by the trafficking of both mono (K⁺) and divalent (Mg²⁺) metal ions, transiently bound in the vicinity of the two-metal-ion catalytic site, at different stages of catalysis (Figure 1B,C). Indeed, the new X-ray structures of the *Bacillus halodurans* RNase H1 in complex with an RNA:DNA hybrid substrate have captured the *in crystallo* intermediates of the catalysis (Figure 1B,C). The active site displays both catalytic Mg²⁺ ions (M_A–M_B) properly located and coordinated by first-shell conserved carboxylates, referred to as the DEDD motif (D71, E109, D132, and D192).

These novel findings support the possible functional role of such transitory metal ions. $^{1,18-23}$ Intriguingly, prior to RNA hydrolysis, two K^+ ions are captured at the active site at different times (Figure 1B). The X-ray structure solved 40 s (40s) after the *in crystallo* incubation shows that a K^+ ion locates at the "U" site (and is hereafter named K_U , PDB ID: 6DMV, Figure S1A). 36 In this position, K_U binds to the catalytic D192 and the phosphate adjacent (P_{ADJ}) to the scissile group (P_{SCI}). Notably, at this stage, no reaction is

Received: April 21, 2021 Revised: June 3, 2021



ACS Catalysis pubs.acs.org/acscatalysis Research Article

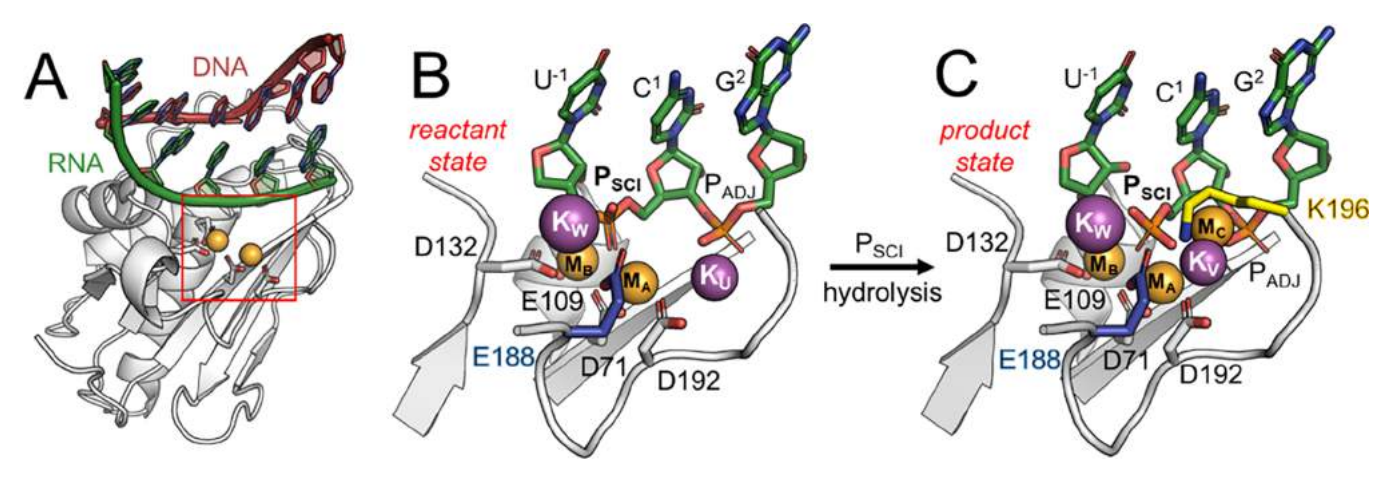


Figure 1. RNase H1 catalytic intermediates captured by time-resolved X-ray crystallography. (A) Overview of the RNase H1 (white) in complex with an RNA:DNA hybrid (green:red). (B) Catalytic site before RNA hydrolysis (i.e., reactant state, PDB ID: 6DO9). The catalytic residues forming the DEDD motif (D71, E109, D132, and D192; white) and the second-shell residue E188 (blue) are represented as sticks. RNA nucleotides (green) including the scissile phosphate (P_{SCI}) and its adjacent phosphate (P_{ADJ}) are also shown. The two catalytic magnesium ions $M_A - M_B$ (orange) and the additional potassium ions K_W and K_U (purple) are shown as spheres. (C) Catalytic site upon RNA hydrolysis (i.e., product state, PDB ID: 6DOX). Here, K_U is replaced by the third divalent metal ion M_C (orange) or by the monovalent K_V (purple), while the second-shell residue K196 (yellow) can directly interact with the scissile phosphate.

observed as the Michaelis-Menten complex is not adequately formed. The distance between Pro-Sp oxygen (O_{Sp}) of the scissile phosphate and the catalytic M_B is 2.6 Å $(dM_B - O_{Sp})$ in Figure S1A, close-up view). Subsequently, after 120 s, a second K⁺ ion locates at the "W" site (viz., K_W, Figure 1B; PDB ID: 6DO9),³⁶ where it is directly coordinated to the second-shell residue E188 and to P_{SCD} in agreement with a previous proposal from classical molecular simulations of this enzyme.³⁴ Notably, at this stage, the scissile phosphate is properly positioned for the catalysis, profiting from the increased vicinity to M_B (with the $dM_B - O_{Sp} = 2.2$ Å, Figure S1B, closeup view). Then, upon RNA hydrolysis, while K_W is still present at the active site (Figure 1C), the occupancy of K_U decreases with product formation. Indeed, after 360 s, a third K+ ion locates very close to the "U" site, at the "V" site (viz., K_V, Figure 1C; PDB ID: 6DOX),³⁶ eventually substituting K_{II}. Moreover, at high concentrations of divalent metals $[M^{2+}]$, a third Mg²⁺ ion is captured to directly coordinate the scissile phosphate at the "C" site (viz., M_C, Figure 1C; PDB ID: 6DPD).³⁶ The *in crystallo* catalysis has also shown that the RNase H1 activity depends on the ionic strength of the reaction buffer.³⁶ Indeed, the formation of reaction products increases with the concentration of both K⁺ and Mg²⁺ cations (i.e., $[K^+]$ and $[Mg^{2+}]$), although an excess of ions leads to the so-called "attenuation effect", which reduces RNA hydrolysis.

Interestingly, catalysis is impaired for the single mutants E188A or K196A in the presence of Mg²⁺.³⁶ The X-ray structures of such mutants have revealed an altered active site architecture as compared to the wild-type (wt) RNase H1 upon RNA hydrolysis, with only partial product formation. In the product structure of the E188A mutant, no K⁺ ion locates at the "W" site (Figure S2A), in contrast to what was observed in the wt form, indicating that E188 directly impacts the presence of K⁺ at the active site. On the other hand, in the structure of the K196A mutant (Figure S2B), one K⁺ ion is captured at the "W" site, as in the wt RNase H1. Nonetheless, in the absence of K196, the products are misfolded due to a slight rotation of the scissile phosphate, in contrast to what was observed in the reactive center of the wt form. Most

importantly, no other $M_{\rm C}$ locates at the active site in this K196A mutant.

Such a wealth of structural and biochemical evidence suggests a functional role of multiple metal ions (K^+ and Mg^{2+}) transiently bound in the vicinity of the two-metal-ion active site in RNase H1, where metal trafficking and exact localization at the reaction center seem critical for catalysis. Indeed, this mechanistic hypothesis would justify the stage-dependent location of additional mono and divalent metals during catalysis, as observed in the *in crystallo* intermediates of RNase H1.

To test this hypothesis and examine the dynamics of this complex stepwise and metal-aided enzymatic process, we applied extensive all-atom molecular dynamics (MD) and free-energy simulations (>27 μ s, in total) on multiple systems of RNase H1 at different stages of the catalysis and ionic strengths of the solution. Our results identify an ordered dynamics of multiple cations and their controlled trafficking at the RNase H1 active site as a functional element of the enzymatic strategy to prompt RNA hydrolysis.

RESULTS

Two Transient K⁺ lons Are Alternatively Located at the Reactants for Catalysis. According to structural data, ³⁶ the RNase H1 catalytic site can contain three K⁺ ions, namely, K_U , K_W , and K_V , which are located at the respective binding site "U", "W", and "V" (Figure 1). The *in crystallo* data also show that this extended K⁺ ion cluster is transiently formed and disrupted during catalysis. Only K_U is initially bound (at 40s, when no reaction is observed, PDB ID: 6DMV). ³⁶ Then, in the reactant state, K_U occupancy decreases, while K_W locates at the active site (at 120 s, PBB ID: 6DO9; at 200 s, PDB ID: 6DOB). Finally, K_W and K_V are found in the products (at 360 s, PDB ID: 6DOX). ³⁶

To investigate K^+ ion's dynamical recruitment and binding at the catalytic site, we first performed two MD simulations of ~ 1 us each, where both K_U and K_W were removed from the reactant state (PDB ID: 6DO9). Such simulations were run at the reference and optimal concentration for catalysis (in line with the experimental conditions of 6 mM $[Mg^{2+}]$ and 200

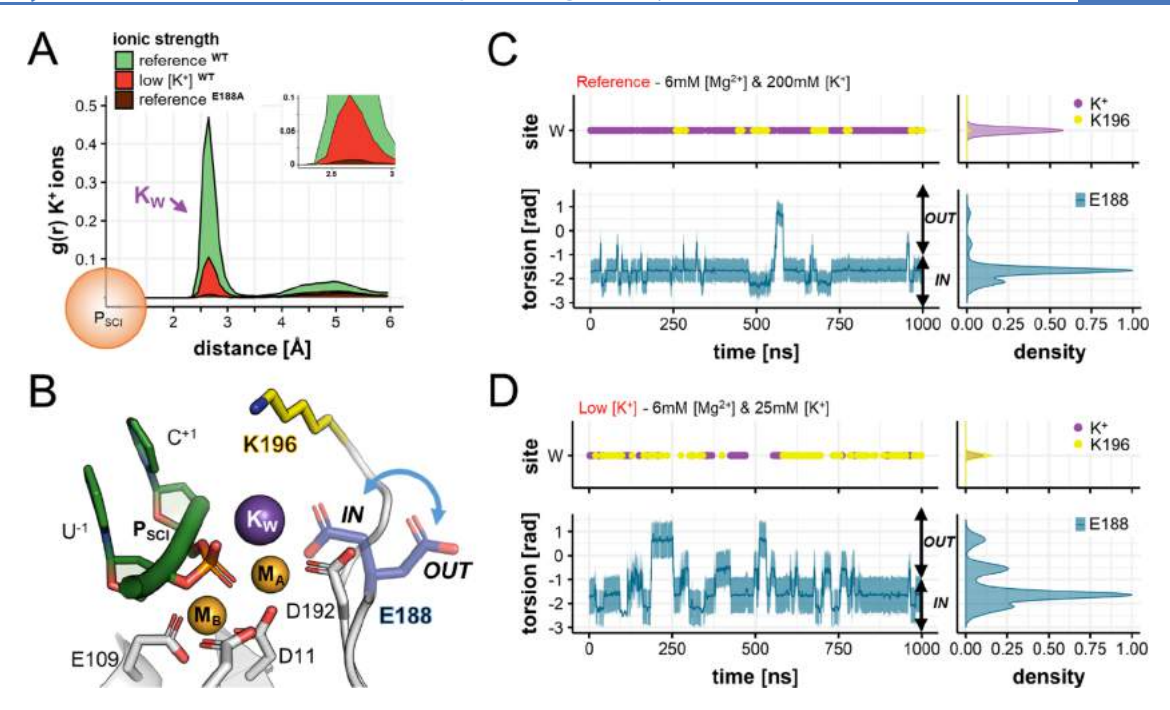


Figure 2. Occupancy of positive charges (i.e., K^+ ions and K196) and conformational dynamics of E188 in the reactant state. (A) Spatial distribution and number of K^+ ions around the scissile phosphate (P_{SCI}) of wild-type RNase H1, computed during MD simulations as the radius of gyration, g(r), for K^+ ions at reference (green) and low (red) K^+ concentrations. In both cases, K^+ ions are mainly found at $\sim 2.77 \pm 0.24$ Å from the scissile phosphate and are thus located at the "W" site. The g(r) for K^+ is also computed during MD simulations of the E188A mutant performed at the reference concentration (brown). Here, the "W" site is never occupied by K^+ ions. (B) Conformational change of the second-shell residue E188 (blue arrow) pointing inside the active site (E188_{IN}) and outside (E188_{OUT}). (C) Occupancy of the "W" site (upper panel) by K^+ ions (purple) and by K196 (yellow) and variation of the torsional angle E188- θ (lower panel, computed between the N-C α -C β -C δ atoms) along MD simulations at reference $[K^+]$. Normalized densities are on the right. At optimal ionic strength, the binding of K^+ is favored and E188 is stabilized in the E188_{IN} conformation. (D) Same descriptors as in (C) for MD simulations at low $[K^+]$. Here, the binding of K_W is disfavored, substituted by K196, and the inner \leftrightarrow outer swings of E188 are more frequent.

mM [K⁺]). First, we noted that, even in the absence of K⁺ ions, the overall catalytic architecture is maintained well (see RMSD in Figure S3). Monitoring the spatial distribution and number of K⁺ ions in a sphere of 6 Å centered on the scissile phosphate (P_{SCI} , Figure 2A), we found that a transient K⁺ ion can be intermittently located at the W site (*i.e.*, K_W). In this position, K_W sits at ~2.77 \pm 0.24 Å from P_{SCI} (Figure S3), in excellent agreement with X-ray data (PDB ID: 6DO9, K_W at = 2.5 Å). On the other hand, K⁺ ions do not occupy the "U" site, which remains empty (Figure 2A and Figure S4A).

We also found that the spontaneous binding of K_w is associated with a conformational change of the second-shell residue E188 (Figure 2B), which can assume two main orientations: pointing toward the active site as in the X-ray structure (viz., E188_{IN}) and outside (viz., E188_{OUT}) toward the bulk. By monitoring the variation of the torsional angle E188-heta(formed by the E188 atoms N-C α -C β -C δ , Figure 2C, lower panel), we found that E188 mainly samples the E188_{IN} state when K_W locates at the "W" site (shown in the upper panel). On the other hand, E188 samples the $E188_{OUT}$ state when the "W" site is not occupied by K_w. This correlation, which is also observed in the simulation replicas (Figure S6), suggests that the inner ↔ outer conformational swing of E188 can favor the recruitment of K+ ions from the bulk to the "W" site. Importantly, these findings are also in agreement with biochemical data showing that catalysis is impaired in the E188A mutant.³⁶ While the active site architecture of this mutant is highly similar to the wt RNase H1 (Figure S2A), the only structural difference is the lack of K_W (PDB ID: 6DPO).³⁶

Accordingly, we further evaluated the role of E188 for the dynamic recruitment of K_W and performed two additional MD simulations (1 μ s, each). First, we simulated the E188A mutant at optimal ionic strength. As a result, no K^+ ions bind at the active site (Figure 2A), at odds with what was observed for the wt RNase H1. This result confirms that the presence of the second-shell E188 promotes the binding of K_W . Then, we performed MD simulations of the wt RNase H1, restraining the E188 residue in the "out" conformation. Here, the occupancy of the "W" site by K^+ ions was dramatically reduced (Figure S6C), suggesting that the inner \leftrightarrow outer conformational swing of E188 is fundamental to guarantee the recruitment and proper positioning of K_W , which thus appears crucial for catalysis.

As noted above, K^+ ions do not occupy the "U" site during such MD simulations. To further corroborate this observation, a third simulation replica has been performed by locating one K^+ ion at the "U" site based on the coordinates of the *in crystallo* RNase H1 intermediate obtained as soon as 40 s after incubation (Figure S1A, PDB ID: 6DMV). Site (Figure S4B), just after the equilibration phase, when the P_{SCI} approaches the M_A-M_B reactive center. That is, the distance between M_B and the Pro-Sp oxygen (O_{Sp}) of the scissile phosphate reaches $dM_B-O_{Sp}=1.9\pm0.13$ Å. Notably, these findings align with the occupancy trend observed for K_U in the series of X-ray structures obtained at different times from incubation. Indeed, the occupancy of K_U (K_U^{Occ}) progressively reduces when the scissile phosphate gets properly

positioned for catalysis and approaches M_B . In detail, at $dM_B - O_{Sp} = 2.6$ Å, $K_U^{\,\,\,\text{Occ}} = 0.35$ (at 40 s, PDB ID: 6DMV); at $dM_B - O_{Sp} = 2.2$ Å, $K_U^{\,\,\,\,\text{Occ}} = 0.25$ (at 120 s, PDB ID: 6DO9); and at $dM_B - O_{Sp} = 2.1$ Å, $K_U^{\,\,\,\,\,\,\,\,\,\,\,\,\,\,\,\,\,\,}$ departure.

Interestingly, the *in crystallo* data also revealed that low [K⁺] led to a reduced product formation in RNase H1.36 We simulated such conditions with three more ~1-\mu s-long MD runs at low K $^+$ concentration (i.e., 6 mM [Mg $^{2+}$] and 25 mM of [K⁺], according to experimental conditions), with both "U" and "W" sites empty. This allowed us to investigate whether a diminished K⁺ ionic strength could affect the recruitment of K⁺ ions at the W site, as well as the dynamical role of E188 in this process. As a result, also at low [K+], we observed null occupancy of the "U" site (Figure 2A and Figure S4A). Moreover, the recruitment of K_W occurs less frequently compared to the simulations at the optimal [K+] (paragraph above), as shown by the decreased occupancy of the "W" site by K⁺ ions (Figure 2A). Most notably, E188 more frequently samples the E188_{OUT} conformation, pointing toward the solvent and searching for a transient K+ ion from the bulk (Figure 2D, lower panel). In this regard, however, it is worth noting that the lack of K_W is often compensated by the positively charged side chain of the second-shell residue K196, which at times accesses the "W" site with almost the same frequency of a K⁺ ion (Figure 2D, upper panel). Overall, MD runs at low [K+] indicate that when K+ does not access the "W" site, E188 preferably assumes the E188_{OUT} state, at odds with MD runs at high $[K^+]$ where the E188_{IN} conformation is mostly observed and $K^{\scriptscriptstyle +}$ occupies the $^{\prime\prime}W^{\prime\prime}$ site. These data corroborate that the binding of K_W is associated with the conformational change of E188, which could act as a K_W functional recruiter.

To further understand the influence of K⁺ concentration on the E188-mediated recruitment of K_W and to estimate the energetics of such process, we performed free-energy simulations using well-tempered metadynamics at both optimal (200 mM) and low (25 mM) [K⁺] (Figure S7). The torsional angle E188- θ was used as a collective variable to sample multiple inner ↔ outer conformational swings of this residue in both directions. At optimal [K+], the free-energy profile for such a conformational switch, when going from E188_{IN} to E188_{OUT} conformations, showed a barrier of \sim 6.2 kcal mol⁻¹, while at low $[K^+]$, it was ~3.7 kcal mol⁻¹ (Figure S7). Additionally, the $E188_{OUT}$ to $E188_{IN}$ conformational swing displayed a barrier of ~ 3.2 kcal mol⁻¹ at optimal [K⁺], while at low $[K^+]$, it was ~2.4 kcal mol⁻¹ (Figure S7). Such low barriers are consistent with the conformational changes observed in our equilibrium simulations. Additionally, the slightly smaller barriers at low $[K^+]$, compared to the barrier at high $[K^+]$, are in line with the result from unbiased MD, overall indicating that a more frequent conformational change of E188 may thus favor the recruitment of one K+ ion from the bulk to the "W"

Finally, four MD simulations of the reactant were performed at high $[Mg^{2+}]$ (80 mM $[Mg^{2+}]$ and 75 mM $[K^+]$, four MD runs of \sim 1 μ s each), which was experimentally shown to reduce RNA hydrolysis through the so-called attenuation effect. ³⁶ In these simulations, although E188 is stabilized in the E188_{IN} conformation, no K^+ ions are captured at the "W" site (Figure S8). This is because an additional Mg^{2+} metal ion

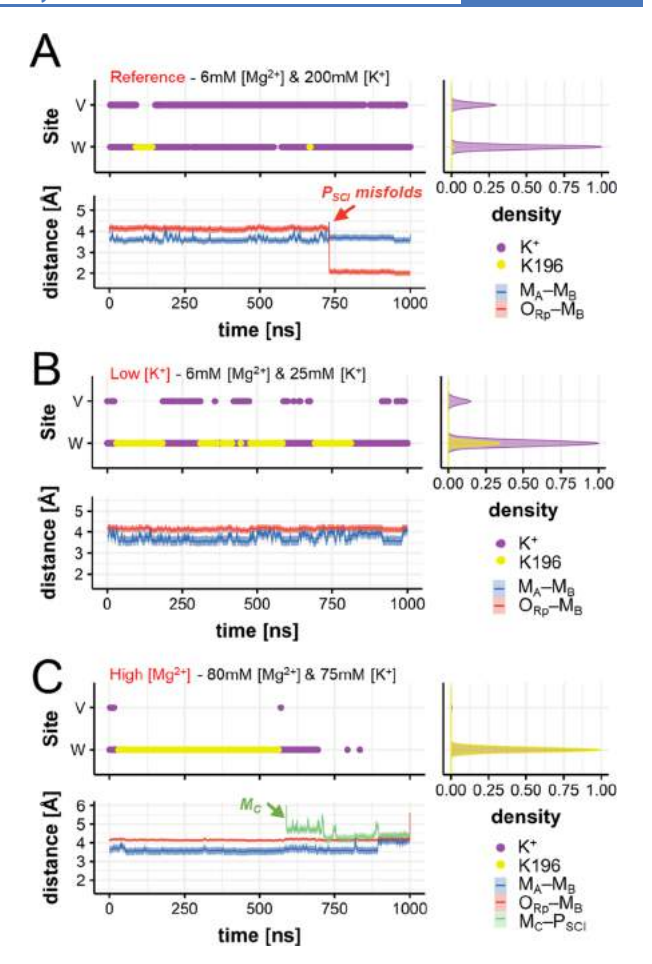


Figure 3. Occupancy of positive charges (viz., K^+ ions and K196) and conformational dynamics of the products. (A) Occupancy of the W and the V sites (upper panel) by K^+ ions (purple) and by the K196 side chain (yellow), and distances (lower panel) between the catalytic ions M_A-M_B (blue trace) and between the pro-Rp oxygen of the scissile phosphate and M_B ($O_{Rp}-M_B$, red trace) during MD at optimal concentrations. Normalized densities are on the right. (B,C) Same descriptors as in (A) for MD simulations at low $[K^+]$ (B) and at high $[Mg^{2+}]$ (C). At low $[K^+]$, the interaction between K196 and the scissile phosphate is more frequent (Figure 4B). At high $[Mg^{2+}]$, M_C approaches the scissile phosphate (green trace of M_C-P_{SCI}), while the M_A-M_B distance increases, preluding the release of the products (Figure 4C).

locates at \sim 4.53 \pm 0.11 Å from the P_{SCI} (Figure S5), close to the "W" site (viz, M_W), and directly binds E188, closing the accessibility of the "W" site to K⁺ ions (Figure S8E). In this way, this third Mg^{2+} ion hampers the dynamic recruitment of K_W , preventing the formation of the K⁺ metal cluster for catalysis at high $[Mg^{2+}]$. This finding may thus represent an explanation of the attenuation effect. 28,37 Notably, these results were confirmed through multiple MD runs using three different nonbonded models for Mg^{2+} (Figure S8). Indeed, although Mg^{2+} parametrization can affect the M_C -E188 binding mode 38 and the dynamics of E188 (Figure S8A–D, lower panel), high $[Mg^{2+}]$ still reduces the E188 inner \leftrightarrow outer conformational switch regardless of the ions' model. In turn, the conformational preference of E188 prevents the E188-mediated recruitment of K_W for catalysis.

Taken together, MD simulations of the reactant state reveal an ordered dynamics of cations, which agrees well with, and adds further clarification to, recent hypotheses based on

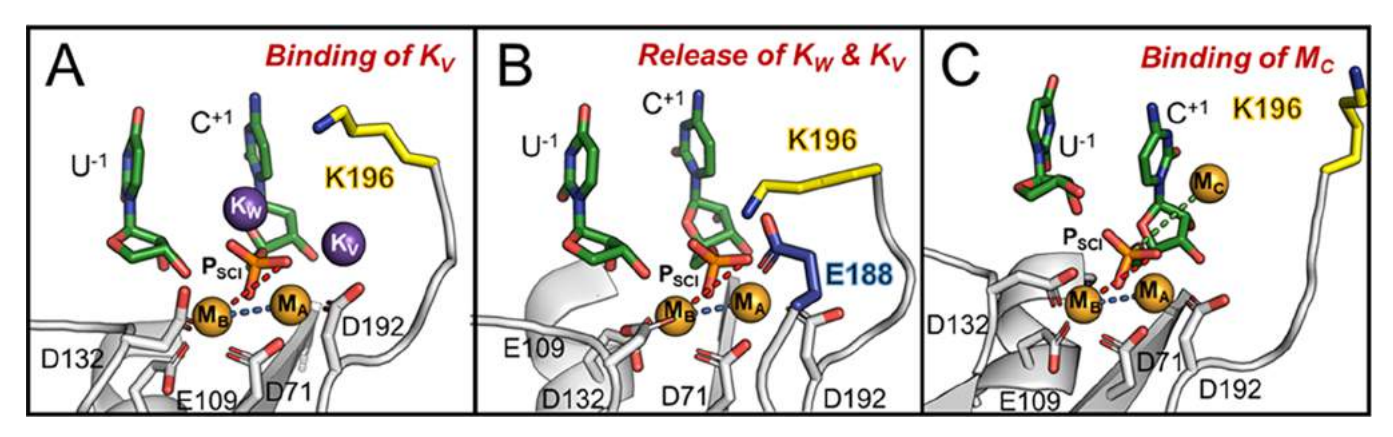


Figure 4. Snapshots of the RNase H1 active site upon catalysis. (A) In the product state, K_W is stably coordinated at the active site, while K_V is only transiently observed. (B) K_W and K_V can exchange their position with K196, which directly coordinates the scissile phosphate preventing its misfolding. (C) The third additional M_C binds the scissile phosphate and promotes the increase of the distance between the two catalytic M_A – M_B ions for product release.

experimental data.³⁶ Accordingly, the catalytic site of RNase H1 initially contains only K_U , which is released just upon the reactants' alignment, so it is prone to catalysis—in general agreement with the mechanistic proposal by Samara and Yang.³⁶ In addition, the simulations reveal an inner \leftrightarrow outer swing of the second-shell residue E188, which is suggested here to critically favor the recruitment of one additional K^+ ion at the "W" site to form the reactant RNase H1 active site. In this way, this sequence of dynamic events, which we show to be optimally controlled by the ionic strength in solution, leads to a competent catalytic state (as in PDB ID: 6DOB).³⁶

Multi K^+ and Mg^{2+} Trafficking Enhances Product Formation. We performed MD simulations of RNase H1 in the product state to evaluate if and how the ionic distribution in the vicinity of the active site is altered upon RNA hydrolysis. The starting configuration included both catalytic metals M_A — M_B and the additional K_W , as observed after 600 s of incubation when the RNA hydrolysis reached a plateau (PDB ID: 6DOG). MD simulations have been performed in analogy with those of the reactant state (previous section) considering an initial reference, *i.e.*, an optimal ionic strength of 6 mM [Mg^{2+}] and 200 mM [K^+].

In these simulations, K_W stably coordinates the scissile phosphate P_{SCI} by locating at the "W" site (Figure 3A, upper panel, and Figure S9A). Moreover, one additional K^+ ion transiently locates at the "V" site (*i.e.*, in the vicinity of the catalytic site but in a distinct position compared to the "W" and "U" sites). In this position, K_V interacts with P_{SCI} (Figure 4A) together with K_W . Importantly, this transient K_V ion superimposes well with the Rb^+ ion observed in the X-ray data (PDB ID: 6DOX). Interestingly, the simulations show that the K196 side chain can also reversibly access the "W" site when empty.

Three additional \sim 1- μ s-long MD runs considered a lower [K⁺] (*i.e.*, 6 mM [Mg²⁺] and 25 mM of [K⁺]). Here, a more frequent interchange between K⁺ and K196 was observed (Figure 3B, upper panel). At lower [K⁺], the "W" and "V" sites are often not occupied by K⁺ compared to their occupancy at higher [K⁺]. Consequently, K196 is more often found to interact directly with the phosphate leaving group (Figure 4B). This results in a stable configuration of the P_{SCI} (Figure 3B, lower panel). On the other hand, when K196 more rarely accesses the "W" site, a partial misfold of the P_{SCI} is observed (Figure 3A, lower panel). These findings, which are well

reproduced in the simulation replicas (Figure S9), suggest that K196 could be quite relevant for the precise accommodation and preliminary departure of the solvent-exposed leaving nucleotides. Indeed, K196 can, at times, interchange with K_W and K_V . As a result, the correct positioning of the phosphate of the leaving group for departure is maintained (as observed in the PDB ID: 6DOG, captured right before leaving group departure). Notably, the positively charged side chain of K196 locates at the W site (at \sim 2.7 Å from P_{SCI}) to H-bond the leaving group only if both K_W and K_V ions have departed from the catalytic site (see Figure S9, where the presence of only K_W still preserves the hydrolyzed leaving group in place at the two-metal-ion center).

Molecular simulations of the products have also been performed at increased $[Mg^{2+}]$ (i.e., 80 mM of Mg^{2+} and 75 mM of K^+ , five MD runs of $\sim 1~\mu s$ each) in line with the experimental conditions. These simulations show that K196 can be replaced by a transient third Mg2+ ion, which locates at the "C" site (viz., M_C , Figure 4C). The approach of M_C consistently occurred in MD replicas, conducted using three different nonbonded models for Mg²⁺ (Figure 3C, lower panel, and S9C,D). This finding matches the structural data obtained at high divalent metal concentrations (≥16 mM), which identified such M_C in a very similar position close to the leaving group (PDB ID: 6DPD). 36 Moreover, upon binding of M_C , the internuclear M_A – M_B distance is increased (from 3.72 \pm 0.11 to ~4.11 \pm 0.07 Å, Figure 3C, lower panel), reflecting the destabilization of the active site's architecture to prelude the products' exit. Thus, such a transient third ion seems recruited in the product state to favor the leaving group departure, as seen in other nucleic acid processing enzymes. 17,39,40

It is important to recall that MD of the reactants at high $[Mg^{2+}]$ have also shown that a third Mg^{2+} ion can locate in the vicinity of the catalytic site (Figures S5 and S8E). In that case, however, the third Mg^{2+} ion locates close to the "W" site and binds E188, hampering the dynamic recruitment of K_W and preventing the formation of the K^+ metal cluster for catalysis. Hence, taken together, the simulations at high $[Mg^{2+}]$ support the idea that a third $M_{\rm C}$ ion could be recruited in the product state to favor the leaving group departure. 17,39,40

These results are also in line with the structure of the K196A mutant (Figure S2B, PDB ID: 6DPM).³⁶ Here, M_C is missing, suggesting that the K196A mutation would somehow impair

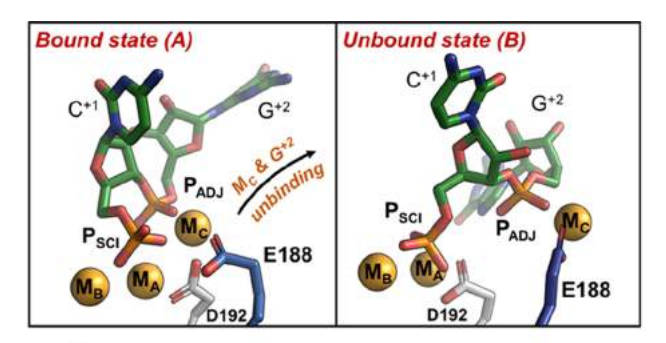
product stabilization, disfavoring M_C recruitment for leaving group departure. To test this hypothesis, we carried out two additional MD runs of the K196A mutant at both low K^+ (*i.e.*, 6 mM [Mg²⁺] and 25 mM [K⁺]) and high Mg²⁺ (*i.e.*, 80 mM [Mg²⁺] and 75 mM [K⁺]) concentrations (~300 ns and ~1 μ s, respectively). These simulations confirm that the K196A mutant does not lead to M_C recruitment, further sustaining the crucial role of K196 for product stabilization and M_C binding (Figure S11).

In summary, molecular simulations of the product state indicate that a controlled metal trafficking at the catalytic site plays a critical role in RNA hydrolysis and product release. Upon RNA hydrolysis, the potassium metal cluster breaks, while K196 contributes to product stabilization before the third divalent $M_{\rm C}$ ion can further favor product release (*vide infra*).

Third Mg^{2+} Trafficking for Product Release. In the products, upon binding of M_C , the internuclear M_A-M_B distance increased (Figure 3C), suggesting that the active site might be prone to release the reaction products, as observed in other two-metal-ion enzymes. ^{17,39,40} To further investigate how the unbinding of the third M_C may facilitate product exit, we performed well-tempered metadynamics simulations of the product state, which comprehends an extended metal cluster formed by M_A-M_B , M_C , and K_W . The Gaussian-shaped potential was deposited using two collective variables (CV_S) : (i) the coordination number of the M_C ion, which traced the number of water molecules in its first shell, and (ii) the distance between M_C and the scissile phosphate $(P_{SCI}-M_C)$.

Metadynamics identifies two main metastable states (viz., A and B, shown in Figure 5, upper panel), which correspond to the two main minima of the computed free-energy surface (FES, Figure 5, lower panel). In state A, M_C bridges the scissile and adjacent phosphates (P_{SCI} and P_{ADI}), while the catalytic D192 and the second-shell E188 establish a monodentate interaction with M_C. In state B, M_C loses the coordination with D192 and gets bidentate coordination with the E188 carboxylic moiety. At this point, the rotation of E188 shuttles the M_C metal out of the active site, together with P_{ADI} , now located \sim 9 Å away from M_A – M_B . Notably, the base G^{+2} and the active site are completely exposed to the bulk, and the distance between the catalytic M_A – M_B reaches ${\sim}4.7$ Å, indicating the opening of the active site for product release. The free-energy barrier estimated on the minimum free-energy path for this process is ~ 15 kcal mol⁻¹, with the unbound state B of \sim 6 kcal mol⁻¹ favored with respect to the bound state A.

We also investigated the role of E188 in the product state via additional metadynamics runs of the E188A mutant (Figure S2A). Remarkably, in these simulations, M_C preserves the coordination with the adjacent phosphate P_{ADJ} and D192 (state A'; Figure S12). However, the absence of the E188 carboxylic moiety, which in the wt RNase H1 functions as an anchoring point for the exit of M_C (Figure 5), strongly disfavors the release mechanism (state B', Figure S12). Indeed, in the E188A mutant, M_C needs first to be partially hydrated before being released together with the products, as shown by the minimum free energy path connecting state A' with B' (Figure S12). Importantly, in this case, the estimated energetic barrier for M_C unbinding and leaving group departure is ~35 kcal mol⁻¹ (Figure S12), more than twice compared to the one obtained for the wt RNase H1. Moreover, in the absence of E188, the bound state A' results favored the unbound state B'



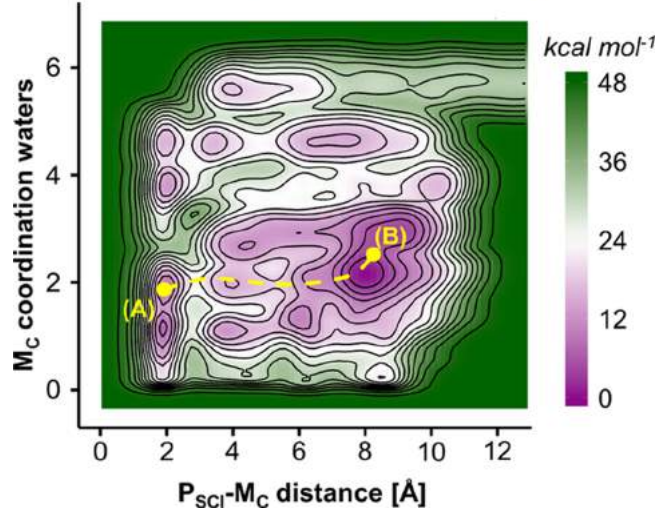


Figure 5. Role of M_C and E188 in the product release. Upper panel: intermediate states (A and B) of the RNase H1 after phosphodiester bond cleavage, identified via free-energy simulations. In state A, M_C is coordinated by E188. Upon rotation of this residue (state B), M_C is released with the departure of the adjacent phosphate (P_{ADJ}). Lower panel: free-energy surface describing the product release mechanism, indicating the two intermediates A and B. The energy scale is in kcal mol⁻¹; contours are traced every 3 kcal mol⁻¹.

of \sim 18 kcal mol⁻¹, as opposed to what was observed in the wt RNase H1.

These results suggest that $M_{\rm C}$ acts in concert with the second-shell residue E188 to promote the release of the reaction products.

DISCUSSION

Controlled Cation Trafficking and Enzymatic Strategy in RNase H1. The RNase H1 enzyme is a fundamental endonuclease involved in DNA replication.²⁵ Recently, timeresolved X-ray crystallography revealed the transient presence of multiple K⁺ and Mg²⁺ ions at the active site of RNase H1 at different stages of catalysis.36 Here, extensive molecular dynamics (MD) and free-energy simulations (over a sampling of >27 μ s) characterized the functional dynamics of this newly determined heteronuclear metal cluster before and upon enzymatic catalysis. Our simulations capture an ordered coordination of motion of transient metal ions and secondshell residues for catalysis. We show that four biding sites in the vicinity of the RNase H1 catalytic core, namely, the "U", "W", "V", and "C" sites (Figure 1), are neatly but only intermittently occupied by K+ and Mg2+ metals during catalysis, in agreement with experiments.

We observed that, before RNA hydrolysis (*i.e.*, in the reactant state), a K^+ ion cluster is dynamically formed to favor

substrate alignment and, possibly, activation for catalysis. At first, one K^+ ion transiently locates at the "U" site (viz, K_U) and assists in forming the catalytically competent fold of the RNase H1 active site. This K_U is spontaneously released into the bulk only after the proper coordination between the scissile phosphate and the two catalytic M_A-M_B ions (Figure S4). At this point, the inner \leftrightarrow outer conformational swing of the second-shell residue E188 favors the recruitment and the precise positioning of a second K^+ ion at the "W" site (viz, K_W , Figure 2), as also observed for enzymes such as human Exo1. In RNase H1, this K_W directly contacts the scissile phosphate to favor the correct positioning of the reactants, prompting catalysis. Such K_W can depolarize the phosphodiester bond, thus promoting the catalytic activation of the reactants. 1,20

Importantly, we found that this chain of dynamic (un)binding events of K+ ions is significantly affected by the reaction buffer's ionic strength. In fact, in agreement with in crystallo data showing that catalysis is reduced at low concentrations of K^+ (i.e., $[K^+]$), 36 MD simulations performed at low [K⁺] show that the E188-mediated recruitment of K_W occurs less frequently (Figure 2D). Accordingly, the inner \leftrightarrow outer conformational swing of E188 is energetically favored at low $[K^+]$ with a barrier of ~ 3.7 kcal mol⁻¹ vs ~ 6.2 kcal mol⁻¹ higher $[K^+]$ (Figure S7). The crucial role observed here for the E188-mediated recruitment of K_w is also sustained by both biochemical and structural evidences. Indeed, alanine mutation of E188 reduces the catalytic efficiency of RNase H1.36 As well, X-ray structures have shown that such mutation displays no K_W at the active site (Figure S2A), at odds with the wt RNase H1.³⁶ In line with this evidence, our MD simulations show that the recruitment of K_W is dramatically hampered when E188 is restrained in its "out" conformation (Figure S6C), as well as when E188 is mutated into an alanine (Figure 2A). These findings support the E188-mediated mechanism for K_W recruitment, which ensures the reactants' proper formation. Notably, these results further corroborate the recruitment role of second-shell residues for two-metal-ion catalysis, such as recently reported for human Exo1, ExoG, Exo-λ, and other 5'exonucleases. 17

Upon RNA hydrolysis, we observe an additional K⁺ ion intermittently located at the so-called "V" site in the vicinity of the catalytic core. This K_V ion coordinates the scissile phosphate P_{SCI} together with K_W (Figures 3A and 4A), as also shown by in crystallo data (PDB ID: 6DOX).³⁶ We note that these K_W/K_V ions can interchange their distinct position with the second-shell residue K196 near P_{SCI} (Figures 3B and 4B). Indeed, such residues favor the stabilization of the P_{SCI}centered reaction products. The functional role of K196 in the products' stabilization is also sustained by the X-ray data of the catalytically impaired K196A mutant of RNase H1 (PDB ID: 6DPM),³⁶ in which the products are misfolded and no third Mg²⁺ ion (M_C) is resolved. Accordingly, MD simulations of this mutant show that the absence of this lysine induces the product's misfolding and hampers the binding of M_C (Figure S11). On the other hand, in the wt RNase H1, leaving group departure occurs when the K⁺ ions and K196 are ultimately displaced by a third Mg²⁺, which spontaneously sits at the "C" site (viz., M_C) and binds P_{SCI} (Figure 4C). At this point, the internuclear M_A – M_B distance is increased (from 3.72 \pm 0.11 to \sim 4.11 \pm 0.07 Å) as the overall active-site structure evolves toward the products (Figures 3C and 4C). This is in line with the X-ray structure showing that the distance between the M_A-M_B increases with product release (PDB ID: 2G8V) from

3.7 to 4.8 Å. From this point, the leaving group departure is expected to occur.

To further investigate the products' release, metadynamics simulations show that M_C is involved in a stepwise product release mechanism. In detail, M_C initially bridges together P_{SCI} and its adjacent phosphate, PADI (Figure 5, state A). In this conformation, M_C functions as a positively charged anchor for E188. At this point, the swing of E188 occurs with the simultaneous departure of the movable M_C together with the reaction products (Figure 5, state B), as also observed for other metalloenzymes. 19,22,42-44 This process occurs with an estimated energy barrier of ~15 kcal mol⁻¹ (Figure 5). Metadynamics simulations of the E188A mutant also confirm such a functional role of E188 for product release. In this case, the estimated energetic barrier for the departure of the leaving group was ~ 35 kcal mol⁻¹ (Figure S12), which is more than 2fold higher than that in the wt RNaseH1. In this regard, we note that, in the human RNase H1, E188 corresponds to H264. Based on both structural and biochemical analvses, 28,29,41 this histidine residue has been proposed to favor, together with the mobile C-terminal loop, the release of the products by altering the coordination of M_A ion (Figure S14).

Such a dynamically controlled trafficking of positive charges at the RNase H1 active site is finely dependent on the specific ion concentration, as displayed in the X-ray experiments. In fact, MD of the reactant performed at higher $[Mg^{2+}]$ showed a third Mg^{2+} ion that spontaneously locates at the "W" site (*viz.*, M_W differently located than M_C , Figure S5), closing the accessibility of the "W" site to K^+ ions. In this location, M_W interacts with E188 (Figure S8E), hampering the E188-mediated recruitment of K_W and preventing the formation of the K^+ metal cluster for catalysis. This mechanistic finding is of particular interest in light of the so-called "attenuation effect". ^{28,37} Indeed, the precise location of this third Mg^{2+} at the "W" site precludes the formation of a catalytic metal cluster, thereby representing an explanation for the reduced RNA hydrolysis at high $[Mg^{2+}]$.

In summary, within the limits of the employed computational approach, our simulations provide a dynamic characterization of metal ion trafficking and its interplay with surrounding residues prior and upon catalysis. These results qualitatively describe an enzymatic strategy in which an extended and heteronuclear cation cluster (K⁺ and Mg²⁺ ions) is dynamically formed and disrupted with the aid of second-shell residues. This mechanism prompts the processing of RNA:DNA hybrids in RNase H1 (Figure 6). That is, the RNase H1 cation trafficking starts with the binding of K_W and K_U , which prompts the alignment of the substrate (Figure 6A). At this point, K_U is released, and the RNA hydrolysis can occur. Upon hydrolysis (i.e., product state, Figure 6B), K_w is assisted by another K_V in neutralizing the negatively charged product. Finally, the exchange of these two K⁺ ions with a third Mg^{2+} ion (viz., M_C) contributes to the product destabilization, leading to the leaving group's release together with M_C (Figure 6C) that precedes the reaction turnover and the continuation of catalysis. Ab initio simulations will now be needed to evaluate the mechanistic and energetic implications of trafficking and strategic localization of such cations for the chemical step of RNA hydrolysis at the reaction center. Nonetheless, our classical simulations indicate that the controlled trafficking of cations, observed over a multimicrosecond sampling, is crucial to promote the formation of

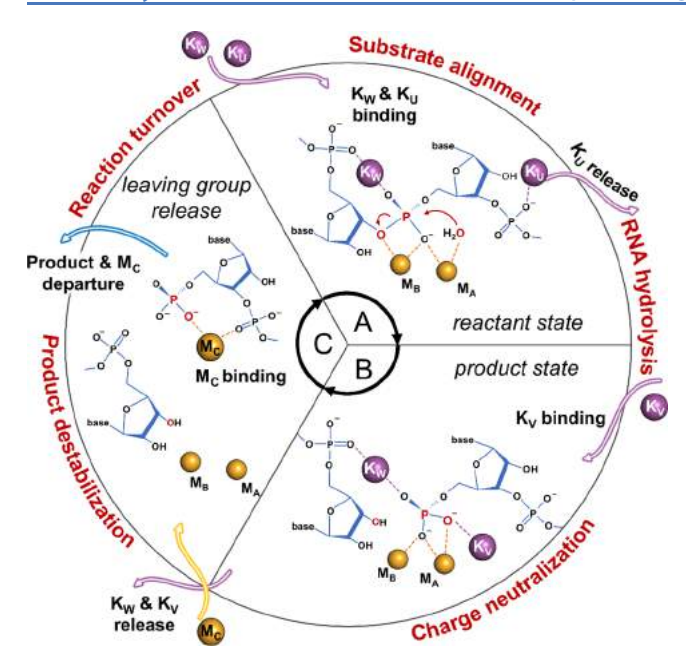


Figure 6. Controlled cation trafficking favors RNase H1 catalysis. (A) In the reactant state, K_W and K_U prompt the alignment of the substrate. At this point, K_U is released and the RNA hydrolysis can occur. (B) Upon hydrolysis (*i.e.*, product state), the negatively charged product is neutralized by K_W and another K_V ion. (C) The ultimate exchange of these two K^+ ions with a third Mg^{2+} ion (*viz.*, M_C) promotes the destabilization of the products, which are then released together with M_C to induce the reaction turnover and the continuation of catalysis.

catalytic states that just precede and follow the enzymatic reaction for substrate hydrolysis.

Similarity of Binding and Trafficking of Metals in Other Nucleic Acid Processing Metalloenzymes. It has been recently shown that conserved and positively charged residues are strategically located at the active core of, e.g., DNA or RNA polymerases and nucleases at conserved sites, expanding the two-metal-ion functional architecture of these enzymes. ^{18,20,40} On this basis, we used structural analyses to investigate whether the mechanistic insights herein provided may be shared among other nucleic acid processing enzymes. We found that the binding sites "U", "W", and "V" transiently occupied by K+ ions in RNase H1 overlap well with secondshell positions occupied by positively charged residues in other enzymes. In fact, the RNase H1 K_W and K_U/K_V, respectively, well superimpose with, e.g., R92 and K85/G2(NH) in human exonuclease 1 (PDB ID: 5V06, Figure S14A)⁵ or with H539 and R557 in HIV-1 reverse transcriptase (PDB ID: 6BSH, Figure S14B), 45 as well as with R100 and K93/G2(NH) in the endonuclease FEN1 (PDB ID: 5UM9, Figure S14C).4

Structural analysis of FEN-1 bringing an alanine mutation of R100 (PDB ID: 5KSE) revealed that, in the absence of R100, an additional metal ion is captured in the same putative "W" site before the catalysis. Hotable similarities also arise from our recent studies investigating the structure and the catalysis of the CRISPR-Cas9 genome editing system. We found that the K970 and R972 residues within the catalytic RuvC domain also transiently engage the so-called "W" and "U/V" binding sites at specific catalytic steps (Figure S14D). Together, these findings support that the trafficking of positive charges at conserved regions of several metalloenzymes is strategically designed and controlled to favor catalysis. In this context, we

note that only one positively charged residue is present in the vicinity of the RNase H1 active site (i.e., K196), contrary to what is found in several other two-metal-ion enzymes. 18,49 This observation may be coupled to the highly solvent-exposed localization of the RNase H1 active site when compared to those mentioned above and second-shell basic residues-rich enzymes (see Figure S15). This may be why the RNase H1 active site shows such prominent trafficking of multications in the lack of multiple strategically located positively charged residues in the surroundings of the enzymatic reaction center. That is, multications binding at the catalytic site may counterbalance the lack of multiple second-shell positively charged residues. As a matter of fact, this would not represent the first example of its kind. Indeed, a similarly extended heteronuclear cluster of movable cations has been captured at the catalytic site of the group II intron ribozymes (two K^+ , K_1 – K₂; and two Mg²⁺ ions, M₁-M₂), RNA-based enzymes that perform RNA hydrolysis in the absence of (positively-charged) aminoacids. 50,51 In group II introns, the position of these ions has been shown to be conserved for catalysis, in analogy with positively charged residues in proteins. 18,52 Importantly, we have recently demonstrated that such a structured metal cluster needs to be dynamically formed and broken to guarantee the proper formation of the introns' catalytic core and favor the release of the reaction products, which matches well with what we uncover herein for RNase H1.53 Moreover, a recent highresolution cryo-EM map of the human spliceosome, 54 which is structurally and chemically related to the group II introns, has revealed the presence of the same conserved heteronuclear metal cluster at its active site, in striking agreement with a model system proposed years before. ^{18,50} Together, this evidence suggests that the controlled trafficking of cations may indeed be a common enzymatic strategy to trigger and assist phosphoryl transfer reactions in living cells, which has been evolutionary conserved and optimized in proteins. In light of these findings and observations, this study shows that finely regulated and controlled trafficking of multiple cations is an essential feature for the enzymatic-mediated hydrolysis of nucleic acids.

CONCLUSIONS

In conclusion, we have used extended atomistic molecular dynamics and free-energy simulations to investigate the cation trafficking recently observed in in crystallo reaction intermediates during catalysis of the RNA ribonuclease H1 (RNase H1) enzyme.³⁶ Our results illustrate a finely regulated trafficking of multiple and diverse cations with functional implications at the reaction center of RNase H1. In agreement with the recent mechanistic hypotheses and experimental data,³⁶ our findings corroborate and sensibly expand the recent notion of an extended two-metal-ion architecture for nucleic acid processing enzymes. 18 Such controlled metal ion trafficking in the vicinity of the catalytic reaction center seems critically designed to aid catalysis in RNase H1 and possibly other similar nucleic acid processing enzymes. Taken together, these findings may encourage further investigations related to enzyme engineering and drug discovery.

■ MATERIALS AND METHODS

Here, the catalytic intermediates of the RNase H1 captured by time-resolved X-ray have been the object of extensive molecular dynamics (MD) and enhanced sampling free-energy

simulations, with the goal of characterizing the dynamics of cation trafficking prior to and upon RNA hydrolysis. Cation trafficking has also been investigated considering the second-shell E188A and K196A mutations and three different ionic strengths of the solution. Overall, we collected a total of >27 μ s of MD multireplica simulations.

Structural Models. To perform MD simulations, six systems were modeled based on the recently time-resolved X-ray structures of Bacillus halodurans RNase H1 in complex with an RNA/DNA hybrid construct.³⁶ First, the reactant state of the wild-type (wt) RNase H1, as obtained from the PDB ID: 6DOG (occupancy C), was considered (Figure 1B). Here, only the crystallized metals M_A-M_B were included in the starting configuration to verify the spontaneous binding events of K+ ions at the "U" and "W" site. Second, the reactant state of the wt RNase H1 included the ions M_A – M_B and K_U , as in PDB ID: 6DMV, to verify the stability of the K_U bound state. Third, the reactant state of the E188A mutant included M_A-M_B, as in PDB ID: 6DPO, to verify the effect of the mutation for the recruitment of K_W. Fourth, we considered the product state of the wt RNAse H1, modeled upon the PDB ID: 6DOG (occupancy B), including the crystalized ions M_A , M_B , and K_W (Figure 1C). Fifth, the product state of the K196A mutant, built on the PDB ID: 6DPM, included the crystallized metals M_A , M_B and K_W (Figure S2B). Sixth, the product state of the E188A mutant, as obtained from the PDB ID: 6DPO, included the crystallized metals M_A, M_B, and M_C (Figure S2A). All the systems were solvated with a layer of water molecules of 15 Å. According to crystallization experiments, each system was simulated at multiple ionic strengths to characterize the effect of the concentrations of the ions on their dynamics. Specifically, Mg²⁺, K⁺, and Cl⁻ ions were added into the simulation boxes to match three different ionic strengths: (i) reference, optimal concentrations, 6 mM [Mg²⁺] and 200 mM [K⁺]; (ii) low K⁺ concentrations, 6 mM [Mg²⁺] and 25 mM [K⁺]; and (iii) high Mg²⁺ concentration, 80 mM [Mg²⁺] and 75 mM [K⁺].

Molecular Simulations. The RNase H1 protein was parametrized with the AMBER force-field ff14SB,555 while the RNA and the DNA of the hybrid were parametrized with the AMBER force-field RNA.OL3⁵⁶⁻⁵⁹ and DNA.OL15.⁶⁰ For the K⁺ metal ions, the parameters of Joung and Cheatham were used. 61,62 The Mg²⁺ ions were systematically modeled according to both 12-6 (Aqvist⁶³ and Allnér⁶⁴) and 12-6-4 (Panteva⁶⁵) nonbonded fixed point charge models to verify that the observed results were independent from the chosen set of parameters. 38,66 Last, the two catalytic Mg^{2+} ions $M_A\!-\!M_B$ were modeled following the atom-in-molecule charges' partitioning scheme⁶⁷ to consider also the charge transfer between the ions and the first-shell coordination residues. The TIP3P model was used for the water molecule.⁶⁸ AMBER^{69,70} was used to perform Langevin⁷¹ MD simulations using an integration time step of 2 fs. The temperature was set at 300 K using a collision frequency $\gamma = 1$ per picosecond, while the constant 1 atm pressure was controlled through a Berendsen barostat⁷² with a relaxation time of 2 ps.

We used the same simulation protocol for all systems. First, we performed an energy minimization to relax the water molecules. At this point, positional restraints of 300 kcal mol- \mathring{A}^2 were imposed on all the heavy atoms of the systems, including the metals. Then, we used a series of NVT and NPT simulations to smoothly thermalize the systems and remove the positional restraints. First, the systems were heated up with

one NVT simulation of \sim 600 ps using the same positional restraints as used during the energy minimization. Subsequently, the positional restraints were progressively halved with a series of two NVT simulations of \sim 200 ps each. Then, two additional simulations in the isothermal—isobaric ensemble (NPT) of \sim 200 ps were performed by further halving the positional restraints, while a third NPT run of \sim 2 ns was performed without any positional restraints to relax the density of the systems to \sim 1.01 g cm $^{-3}$. Last, we performed multiple-replica production runs to collect overall \sim 27 μ s of simulation time. Specifically, we collected \sim 13 μ s for the prereactive state of the wild type, 13 replicas; \sim 9 μ s for the post-reactive state of the wild type, 13 replicas; and \sim 1.3 μ s for the post-reactive state of the K196A mutants, two replicas.

Metadynamics. Two independent metadynamics simulations were performed to characterize the conformational change of E188 in the pre-reactive state. To ensure the convergence of the calculations, we used the well-tempered variant, ⁷³ setting the temperature at 300 K and the bias factor at 8. The Gaussian-shaped potential (height = 1.2 kJ mol⁻¹, width = 0.35 *rad.*) was added with a frequency of 0.5 ps on the torsional angle E188- θ (between the E188 atoms N-C α -C β -C δ). Overall, we collected ~400 ns at both high and low K⁺ concentrations.

Additional well-tempered metadynamics simulations were performed to elucidate the release of the $M_{\rm C}$ metal and the reaction products. The post-reactive state of both the wild type and the E188A mutant was used as starting configurations for the two independent simulations. Here, the temperature was set to 300 K and the bias factor was set to 15. The coordination number of the $M_{\rm C}$, which defines the number of water molecules in the first coordination shell, and the distance between the scissile phosphate and the $M_{\rm C}$ were used as collective variables (CV1 and CV2, respectively). The Gaussian-shaped potential was added with a frequency of 0.2 ps on both the CV1 (height = 0.3 kJ mol⁻¹, width = 0.1) and CV2 (height = 0.3 kJ mol⁻¹, width = 0.5 Å).

ASSOCIATED CONTENT

Supporting Information

The Supporting Information is available free of charge at https://pubs.acs.org/doi/10.1021/acscatal.1c01825.

Supplementary figures reporting the: (i) analysis of structural data (Figures S1, S2, S15, and S16), (ii) indepth analysis of the results obtained from multiple simulations replicas (Figures S3–S6 and S8–S11), and (ii) results from metadynamics simulations (Figures S7 and S12–S14) (PDF)

AUTHOR INFORMATION

Corresponding Authors

Marco De Vivo — Laboratory of Molecular Modelling & Drug Discovery, Istituto Italiano di Tecnologia, Genoa 16163, Italy; ⊚ orcid.org/0000-0003-4022-5661; Email: marco.devivo@iit.it

Giulia Palermo — Department of Bioengineering and Department of Chemistry, University of California Riverside, Riverside, California 52512, United States; orcid.org/0000-0003-1404-8737; Email: giulia.palermo@ucr.edu

Author

Jacopo Manigrasso — Laboratory of Molecular Modelling & Drug Discovery, Istituto Italiano di Tecnologia, Genoa 16163, Italy; Department of Bioengineering, University of California Riverside, Riverside, California 52512, United States; orcid.org/0000-0003-4076-8930

Complete contact information is available at: https://pubs.acs.org/10.1021/acscatal.1c01825

Notes

The authors declare no competing financial interest.

ACKNOWLEDGMENTS

The manuscript was written through contributions of all authors. We thank all members of the Palermo and De Vivo Labs for helpful discussions. Research reported in this publication was supported by the National Science Foundation under Grant CHE-1905374 [to G.P.] and by the National Institute of General Medical Sciences of the National Institutes of Health under Award R01GM141329 [to G.P.]. Computer time has been awarded by XSEDE [grant TG-MCB160059 to G.P.] and by NERSC [grant M3807 to G.P.]. M.D.V. thanks the Italian Association for Cancer Research (AIRC) for financial support [IG 23679].

REFERENCES

- (1) Gao, Y.; Yang, W. Capture of a Third Mg2+ Is Essential for Catalyzing DNA Synthesis. *Science* **2016**, 352, 1334–1337.
- (2) Nakamura, T.; Zhao, Y.; Yamagata, Y.; Hua, Y. J.; Yang, W. Watching DNA Polymerase η Make a Phosphodiester Bond. *Nature* **2012**, 487, 196–201.
- (3) Uson, M. L.; Carl, A.; Goldgur, Y.; Shuman, S. Crystal Structure and Mutational Analysis of Mycobacterium Smegmatis FenA Highlight Active Site Amino Acids and Three Metal Ions Essential for Flap Endonuclease and 5 Exonuclease Activities. *Nucleic Acids Res.* **2018**, *46*, 4164–4175.
- (4) Prieto, J.; Redondo, P.; Merino, N.; Villate, M.; Montoya, G.; Blanco, F. J.; Molina, R. Structure of the I-SceI Nuclease Complexed with Its DsDNA Target and Three Catalytic Metal Ions. *Acta Crystallogr., Sect. F: Struct. Biol. Commun.* **2016**, *72*, 473–479.
- (5) Shi, Y.; Hellinga, H. W.; Beese, L. S. Interplay of Catalysis, Fidelity, Threading, and Processivity in the Exo- and Endonucleolytic Reactions of Human Exonuclease I. *Proc. Natl. Acad. Sci. U. S. A.* **2017**, *114*, 6010–6015.
- (6) Yang, W. Nucleases: Diversity of Structure, Function and Mechanism. Q. Rev. Biophys. 2011, 44, 1.
- (7) Palermo, G.; Cavalli, A.; Klein, M. L.; Alfonso-Prieto, M.; Dal Peraro, M.; De Vivo, M. Catalytic Metal Ions and Enzymatic Processing of DNA and RNA. Acc. Chem. Res. 2015, 48, 220–228.
- (8) Palermo, G.; Stenta, M.; Cavalli, A.; Dal Peraro, M.; De Vivo, M. Molecular Simulations Highlight the Role of Metals in Catalysis and Inhibition of Type II Topoisomerase. *J. Chem. Theory Comput.* **2013**, *9*, 857–862.
- (9) Schmidt, B. H.; Burgin, A. B.; Deweese, J. E.; Osheroff, N.; Berger, J. M. A Novel and Unified Two-Metal Mechanism for DNA Cleavage by Type II and IA Topoisomerases. *Nature* **2010**, *465*, 641–644.
- (10) Nishino, T.; Morikawa, K. Structure and Function of Nucleases in DNA Repair: Shape, Grip and Blade of the DNA Scissors. *Oncogene* **2002**, *21*, 9022–9032.
- (11) Potapov, V.; Fu, X.; Dai, N.; Corrêa, I. R., Jr.; Tanner, N. A.; Ong, J. L. Base Modifications Affecting RNA Polymerase and Reverse Transcriptase Fidelity. *Nucleic Acids Res.* **2018**, *46*, 5753–5763.
- (12) Pavlov, Y. I.; Shcherbakova, P. V.; Rogozin, I. B. Roles of DNA Polymerases in Replication, Repair, and Recombination in Eukaryotes. *Int. Rev. Cytol.* **2006**, 255, 41–132.

- (13) Pommier, Y. Drugging Topoisomerases: Lessons and Challenges. ACS Chem. Biol. 2013, 8, 82-95.
- (14) Arencibia, J. M.; Brindani, N.; Franco-Ulloa, S.; Nigro, M.; Kuriappan, J. A.; Ottonello, G.; Bertozzi, S. M.; Summa, M.; Girotto, S.; Bertorelli, R.; Armirotti, A.; De Vivo, M. Design, Synthesis, Dynamic Docking, Biochemical Characterization, and in Vivo Pharmacokinetics Studies of Novel Topoisomerase II Poisons with Promising Antiproliferative Activity. *J. Med. Chem.* **2020**, *63*, 3508–3521
- (15) Zheng, L.; Jia, J.; Finger, L. D.; Guo, Z.; Zer, C.; Shen, B. Functional Regulation of FEN1 Nuclease and Its Link to Cancer. *Nucleic Acids Res.* **2011**, *39*, 781–794.
- (16) Riccardi, L.; Genna, V.; De Vivo, M. Metal-Ligand Interactions in Drug Design. *Nat. Rev. Chem.* **2018**, 2, 100-112.
- (17) Donati, E.; Genna, V.; De Vivo, M. Recruiting Mechanism and Functional Role of a Third Metal Ion in the Enzymatic Activity of 5' Structure-Specific Nucleases. *J. Am. Chem. Soc.* **2020**, *142*, 2823–2834
- (18) Genna, V.; Colombo, M.; De Vivo, M.; Marcia, M. Second-Shell Basic Residues Expand the Two-Metal-Ion Architecture of DNA and RNA Processing Enzymes. *Structure* **2018**, *26*, 40–50.e2.
- (19) Perera, L.; Freudenthal, B. D.; Beard, W. A.; Shock, D. D.; Pedersen, L. G.; Wilson, S. H.; Broyde, S. Requirement for Transient Metal Ions Revealed through Computational Analysis for DNA Polymerase Going in Reverse. *Proc. Natl. Acad. Sci. U. S. A.* **2015**, *112*, E5228–E5236.
- (20) Genna, V.; Donati, E.; De Vivo, M. The Catalytic Mechanism of DNA and RNA Polymerases. ACS Catal. 2018, 8, 11103–11118.
- (21) Genna, V.; Carloni, P.; De Vivo, M. A Strategically Located Arg/Lys Residue Promotes Correct Base Paring during Nucleic Acid Biosynthesis in Polymerases. *J. Am. Chem. Soc.* **2018**, *140*, 3312–3321.
- (22) Stevens, D. R.; Hammes-Schiffer, S. Exploring the Role of the Third Active Site Metal Ion in DNA Polymerase η with QM/MM Free Energy Simulations. *J. Am. Chem. Soc.* **2018**, *140*, 8965–8969.
- (23) Yang, W.; Weng, P. J.; Gao, Y. A New Paradigm of DNA Synthesis: Three-Metal-Ion Catalysis. *Cell Biosci.* **2016**, *6*, 51–57.
- (24) Borišek, J.; Magistrato, A. An Expanded Two-Zn²⁺ -Ion Motif Orchestrates Pre-MRNA Maturation in the 3'-End Processing Endonuclease Machinery. ACS Catal. **2021**, 11, 4319–4326.
- (25) Broccoli, S.; Rallu, F.; Sanscartler, P.; Cerritelli, S. M.; Crouch, R. J.; Drolet, M. Effects of RNA Polymerase Modifications on Transcription-Induced Negative Supercoiling and Associated R-Loop Formation. *Mol. Microbiol.* **2004**, *52*, 1769–1779.
- (26) Cerritelli, S. M.; Crouch, R. J. Ribonuclease H: The Enzymes in Eukaryotes. *FEBS J.* **2009**, *276*, 1494–1505.
- (27) Tadokoro, T.; Kanaya, S. Ribonuclease H: Molecular Diversities, Substrate Binding Domains, and Catalytic Mechanism of the Prokaryotic Enzymes. *FEBS J.* **2009**, 276, 1482–1493.
- (28) Nowotny, M.; Gaidamakov, S. A.; Crouch, R. J.; Yang, W. Crystal Structures of RNase H Bound to an RNA/DNA Hybrid: Substrate Specificity and Metal-Dependent Catalysis. *Cell* **2005**, *121*, 1005–1016.
- (29) Nowotny, M.; Gaidamakov, S. A.; Ghirlando, R.; Cerritelli, S. M.; Crouch, R. J.; Yang, W. Structure of Human RNase H1 Complexed with an RNA/DNA Hybrid: Insight into HIV Reverse Transcription. *Mol. Cell* **2007**, 28, 264–276.
- (30) Yang, W.; Hendrickson, W. A.; Crouch, R. J.; Satow, Y. Structure of Ribonuclease H Phased at 2 A Resolution by MAD Analysis of the Selenomethionyl Protein. *Science* **1990**, *249*, 1398–1405
- (31) Nowotny, M.; Cerritelli, S. M.; Ghirlando, R.; Gaidamakov, S. A.; Crouch, R. J.; Yang, W. Specific Recognition of RNA/DNA Hybrid and Enhancement of Human RNase H1 Activity by HBD. *EMBO J.* **2008**, *27*, 1172–1181.
- (32) Champoux, J. J.; Schultz, S. J. Ribonuclease H: Properties, Substrate Specificity and Roles in Retroviral Reverse Transcription. *FEBS J.* **2009**, 276, 1506–1516.

- (33) De Vivo, M.; Dal Peraro, M.; Klein, M. L. Phosphodiester Cleavage in Ribonuclease H Occurs via an Associative Two-Metal-Aided Catalytic Mechanism. *J. Am. Chem. Soc.* **2008**, *130*, 10955–10962.
- (34) Ho, M. H.; De Vivo, M.; Dal Peraro, M.; Klein, M. L. Understanding the Effect of Magnesium Ion Concentration on the Catalytic Activity of Ribonuclease H through Computation: Does a Third Metal Binding Site Modulate Endonuclease Catalysis? *J. Am. Chem. Soc.* **2010**, *132*, 13702–13712.
- (35) Rosta, E.; Nowotny, M.; Yang, W.; Hummer, G. Catalytic Mechanism of RNA Backbone Cleavage by Ribonuclease H from Quantum Mechanics/Molecular Mechanics Simulations. *J. Am. Chem. Soc.* **2011**, *133*, 8934–8941.
- (36) Samara, N. L.; Yang, W. Cation Trafficking Propels RNA Hydrolysis. *Nat. Struct. Mol. Biol.* **2018**, 25, 715–721.
- (37) Keck, J. L.; Goedken, E. R.; Marqusee, S. Activation/Attenuation Model for RNase H. J. Biol. Chem. 1998, 273, 34128–34133.
- (38) Panteva, M. T.; Giambaşu, G. M.; York, D. M. Comparison of Structural, Thermodynamic, Kinetic and Mass Transport Properties of Mg2+ Ion Models Commonly Used in Biomolecular Simulations. *J. Comput. Chem.* **2015**, *36*, 970–982.
- (39) Genna, V.; Vidossich, P.; Ippoliti, E.; Carloni, P.; De Vivo, M. A Self-Activated Mechanism for Nucleic Acid Polymerization Catalyzed by DNA/RNA Polymerases. *J. Am. Chem. Soc.* **2016**, *138*, 14592–14598.
- (40) Genna, V.; Gaspari, R.; Dal Peraro, M.; De Vivo, M. Cooperative Motion of a Key Positively Charged Residue and Metal Ions for DNA Replication Catalyzed by Human DNA Polymerase-n. Nucleic Acids Res. 2016, 44, 2827–2836.
- (41) Nowotny, M.; Yang, W. Stepwise Analyses of Metal Ions in RNase H Catalysis from Substrate Destabilization to Product Release. *EMBO J.* **2006**, *25*, 1924–1933.
- (42) Golosov, A. A.; Warren, J. J.; Beese, L. S.; Karplus, M. The Mechanism of the Translocation Step in DNA Replication by DNA Polymerase I: A Computer Simulation Analysis. *Structure* **2010**, *18*, 83–93.
- (43) Da, L. T.; Pardo Avila, F.; Wang, D.; Huang, X. A Two-State Model for the Dynamics of the Pyrophosphate Ion Release in Bacterial RNA Polymerase. *PLoS Comput. Biol.* **2013**, *9*, e1003020.
- (44) Yoon, H.; Warshel, A. Simulating the Fidelity and the Three Mg Mechanism of Pol η and Clarifying the Validity of Transition State Theory in Enzyme Catalysis. *Proteins: Struct. Funct. Bioinf.* **2017**, 85, 1446–1453.
- (45) Tian, L.; Kim, M. S.; Li, H.; Wang, J.; Yang, W. Structure of HIV-1 Reverse Transcriptase Cleaving RNA in an RNA/DNA Hybrid. *Proc. Natl. Acad. Sci. U. S. A.* 2018, 115, 507–512.
- (46) Tsutakawa, S. E.; Thompson, M. J.; Arvai, A. S.; Neil, A. J.; Shaw, S. J.; Algasaier, S. I.; Kim, J. C.; Finger, L. D.; Jardine, E.; Gotham, V. J. B.; Sarker, A. H.; Her, M. Z.; Rashid, F.; Hamdan, S. M.; Mirkin, S. M.; Grasby, J. A.; Tainer, J. A. Phosphate Steering by Flap Endonuclease 1 Promotes 5'-Flap Specificity and Incision to Prevent Genome Instability. *Nat. Commun.* **2017**, *8*, 1–14.
- (47) Palermo, G. Structure and Dynamics of the CRISPR-Cas9 Catalytic Complex. J. Chem. Inf. Model. 2019, 59, 2394-2406.
- (48) Casalino, L.; Nierzwicki, Ł.; Jinek, M.; Palermo, G. Catalytic Mechanism of Non-Target DNA Cleavage in CRISPR-Cas9 Revealed by Ab Initio Molecular Dynamics. *ACS Catal.* **2020**, *10*, 13596–13605.
- (49) Vidossich, P.; Castañeda Moreno, L. E.; Mota, C.; de Sanctis, D.; Miscione, G. P.; De Vivo, M. Functional Implications of Second-Shell Basic Residues for DUTPase DR2231 Enzymatic Specificity. *ACS Catal.* **2020**, 13825–13833.
- (50) Palermo, G.; Casalino, L.; Magistrato, A.; McCammon, J. A. Understanding the mechanistic basis of non-coding RNA through molecular dynamics simulations. *J. Struct. Biol.* **2019**, *109*, 267–279. (51) Casalino, L.; Palermo, G.; Rothlisberger, U.; Magistrato, A. Who Activates the Nucleophile in Ribozyme Catalysis? An Answer

- from the Splicing Mechanism of Group II Introns. J. Am. Chem. Soc. 2016, 138, 10374–10377.
- (52) Genna, V.; Marcia, M.; De Vivo, M. A Transient and Flexible Cation-IIInteraction Promotes Hydrolysis of Nucleic Acids in DNA and RNA Nucleases. *J. Am. Chem. Soc.* **2019**, *141*, 10770–10776.
- (53) Manigrasso, J.; Chillón, I.; Genna, V.; Vidossich, P.; Somarowthu, S.; Pyle, A. M.; De Vivo, M.; Marcia, M. Visualizing Group II Intron Dynamics between the First and Second Steps of Splicing. *Nat. Commun.* **2020**, *11*, 2837.
- (54) Wilkinson, M. E.; Fica, S. M.; Galej, W. P.; Nagai, K. Structural Basis for Conformational Equilibrium of the Catalytic Spliceosome. *Mol. Cell* **2021**, 1–1452.e9.
- (55) Maier, J. A.; Martinez, C.; Kasavajhala, K.; Wickstrom, L.; Hauser, K. E.; Simmerling, C. Ff14SB: Improving the Accuracy of Protein Side Chain and Backbone Parameters from Ff99SB. *J. Chem. Theory Comput.* **2015**, *11*, 3696–3713.
- (56) Darian, E.; Gannett, P. M. Application of Molecular Dynamics Simulations to Spin-Labeled Oligonucleotides. *J. Biomol. Struct. Dyn.* **2005**, *22*, 579–593.
- (57) Wang, J.; Cieplak, P.; Kollman, P. A. How Well Does a Restrained Electrostatic Potential (RESP) Model Perform in Calculating Conformational Energies of Organic and Biological Molecules? *J. Comput. Chem.* **2000**, *21*, 1049–1074.
- (58) Pérez, A.; Marchán, I.; Svozil, D.; Sponer, J.; Cheatham, T. E., III; Laughton, C. A.; Orozco, M. Refinement of the AMBER Force Field for Nucleic Acids: Improving the Description of α/γ Conformers. *Biophys. J.* **2007**, *92*, 3817–3829.
- (59) Zgarbová, M.; Otyepka, M.; Šponer, J.; Mládek, A.; Banáš, P.; Cheatham, T. E.; Jurečka, P. Refinement of the Cornell et Al. Nucleic Acids Force Field Based on Reference Quantum Chemical Calculations of Glycosidic Torsion Profiles. *J. Chem. Theory Comput.* **2011**, *7*, 2886–2902.
- (60) Galindo-Murillo, R.; Robertson, J. C.; Zgarbová, M.; Šponer, J.; Otyepka, M.; Jurečka, P.; Cheatham, T. E. Assessing the Current State of Amber Force Field Modifications for DNA. *J. Chem. Theory Comput.* **2016**, *12*, 4114–4127.
- (61) Joung, I. S.; Cheatham, T. E., III Determination of Alkali and Halide Monovalent Ion Parameters for Use in Explicitly Solvated Biomolecular Simulations. *J. Phys. Chem. B* **2008**, *112*, 9020–9041.
- (62) Joung, I. S.; Cheatham, T. E., III Molecular Dynamics Simulations of the Dynamic and Energetic Properties of Alkali and Halide Ions Using Water-Model-Specific Ion Parameters. *J. Phys. Chem. B* **2009**, *113*, 13279–13290.
- (63) Åqvist, J. Ion-Water Interaction Potentials Derived from Free Energy Perturbation Simulations. *J. Phys. Chem.* **1990**, *94*, 8021–8024.
- (64) Allnér, O.; Nilsson, L.; Villa, A. Magnesium Ion-Water Coordination and Exchange in Biomolecular Simulations. *J. Chem. Theory Comput.* **2012**, *8*, 1493–1502.
- (65) Panteva, M. T.; Giambaşu, G. M.; York, D. M. Force Field for Mg2+, Mn2+, Zn2+, and Cd2+ Ions That Have Balanced Interactions with Nucleic Acids. *J. Phys. Chem. B* **2015**, *119*, 15460–15470.
- (66) Casalino, L.; Palermo, G.; Abdurakhmonova, N.; Rothlisberger, U.; Magistrato, A. Development of Site-Specific Mg2+-RNA Force Field Parameters: A Dream or Reality? Guidelines from Combined Molecular Dynamics and Quantum Mechanics Simulations. *J. Chem. Theory Comput.* **2017**, *13*, 340–352.
- (67) Dal Peraro, M.; Spiegel, K.; Lamoureux, G.; De Vivo, M.; DeGrado, W. F.; Klein, M. L. Modeling the Charge Distribution at Metal Sites in Proteins for Molecular Dynamics Simulations. *J. Struct. Biol.* **2007**, *157*, 444–453.
- (68) Jorgensen, W. L.; Chandrasekhar, J.; Madura, J. D.; Impey, R. W.; Klein, M. L. Comparison of Simple Potential Functions for Simulating Liquid Water. *J. Chem. Phys.* **1983**, *79*, 926–935.
- (69) Case, D. A.; Belfon, K.; Ben-Shalom, I. Y.; Brozell, S. R.; Cerutti, D. S.; Cheatham, T. E., III; Cruzeiro, V. W. D.; Darden, T. A.; Duke, R. E.; Giambasu, G.; Gilson, M. K.; Gohlke, H.; Goetz, A. W.; Harris, R.; Izadi, S.; Izmailov, S. A.; Kasavajhala, K.; Kovalenko, A.; Krasny, R.; Kurtzman, T.; Lee, T. S.; LeGrand, S.; Li, P.; Lin, C.; Liu,

- J.; Luchko, T.; Luo, R.; Man, V.; Merz, K. M.; Miao, Y.; Mikhailovskii, O.; Monard, G.; Nguyen, H.; Onufriev, A.; Pan, F.; Pantano, S.; Qi, R.; Roe, D.R.; Roitberg, A.; Sagui, C.; Schott-Verdugo, S.; Shen, J.; Simmerling, C.L.; Skrynnikov, N. R.; Smith, J.; Swails, J.; Walker, R. C.; Wang, J.; Wilson, L.; Wolf, R. M.; Wu, X.; Xiong, Y.; Xue, Y.; York, D. M.; Kollman, P. A. AMBER; Univ. California: San Fr, 2018. (70) Lee, T. S.; Cerutti, D. S.; Mermelstein, D.; Lin, C.; Legrand, S.; Giese, T. J.; Roitberg, A.; Case, D. A.; Walker, R. C.; York, D. M. GPU-Accelerated Molecular Dynamics and Free Energy Methods in Amber18: Performance Enhancements and New Features. J. Chem. Inf. Model. 2018, 58, 2043–2050.
- (71) Turq, P.; Lantelme, F.; Friedman, H. L. Brownian Dynamics: Its Application to Ionic Solutions. *J. Chem. Phys.* **1977**, *66*, 3039–3044.
- (72) Berendsen, H. J. C.; Postma, J. P. M.; Van Gunsteren, W. F.; Dinola, A.; Haak, J. R. Molecular Dynamics with Coupling to an External Bath. *J. Chem. Phys.* **1984**, *81*, 3684–3690.
- (73) Barducci, A.; Bussi, G.; Parrinello, M. Well-Tempered Metadynamics: A Smoothly Converging and Tunable Free-Energy Method. *Phys. Rev. Lett.* **2008**, *100*, 1–4.